INTERNATIONAL JOURNAL FOR NUMERICAL METHODS IN ENGINEERING
Int. J. Numer. Meth. Engng 2007; **70**:728–755
Published online 24 October 2006 in Wiley InterScience (www.interscience.wiley.com). DOI: 10.1002/nme.1907

A fixed-mesh Eulerian–Lagrangian approach for stress analysis in continuous casting

Víctor D. Fachinotti and Alberto Cardona*, †

Centro Internacional de Métodos Computacionales en Ingeniería (CIMEC-INTEC), Universidad Nacional del Litoral-Conicet, Güemes 3450, CP 3000 Santa Fe, Argentina

SUMMARY

We present a method for the analysis of the strains and stresses developed in the solidified portion of a metal strand during the continuous casting process. Steady-state conditions are assumed. The solidified metal is modelled as a standard inelastic solid with isotropic hardening and von Mises yield criterion. Constitutive equations are formulated over the material particles (Lagrangian approach) that instantaneously occupy a fixed domain attached to the casting machine, which is discretized (Eulerian approach). Particle tracking, needed to record the deformation history at each fixed sampling point, becomes trivial because of the usual hypothesis of constant and homogeneous advection velocity. Backward-Euler (implicit) finite differences and mixed finite elements are used for time and spatial discretization, respectively. The resulting non-linear algebraic equations are solved using the Newton–Raphson method. Copyright © 2006 John Wiley & Sons, Ltd.

Received 19 July 2005; Revised 10 September 2006; Accepted 11 September 2006

KEY WORDS: solids; finite element methods; materials science; phase change; thermal stresses; continuous casting

1. INTRODUCTION

Leaving aside particular design details, continuous casting consists in pouring liquid metal into an open-chilled mould. The mould should remove enough superheat and latent heat from the melt in order to form a solidified shell capable of containing the liquid inside at the mould exit. Below

*Correspondence to: Alberto Cardona, CIMEC-INTEC, Güemes 3450, CP 3000 Santa Fe, Argentina.
†E-mail: acardona@intec.unl.edu.ar

Contract/grant sponsor: Agencia Nacional de Promoción Científica y Tecnológica; contract/grant number: PID 99-76
Contract/grant sponsor: Consejo Nacional de Investigaciones Científicas y Técnicas; contract/grant number: PIP 5271
Contract/grant sponsor: Universidad Nacional del Litoral; contract/grant number: CAI + D PE 214

the mould, the strand is driven between support rolls through the secondary cooling region where it is further cooled *via* water spraying.

We assume the process has reached steady-state conditions for the purpose of the current analysis. Therefore, we are not concerned with start-up problems or any other transient phenomena, such as mould oscillation, meniscus fluctuation, etc.

The strand cooling is not uniform, which leads to thermal gradients that induce thermal strains. Since the strand deformation is constrained by the mould, this also causes thermal stresses within the solidified material. Proper modelling of such phenomena requires an accurate description of the complex relations among stresses, strains and time at high temperature. Indeed, the mechanical behaviour of metals within the temperature range involved in continuous casting is highly inelastic, i.e. the state of any material particle at any time depends on the entire deformation history experienced by the considered particle up to this time.

Historically, the Lagrangian kinematics description—based on material particles—has provided the most convenient way to compute stresses in inelastic bodies. However, the Lagrangian description requires to follow the strand as it moves down the caster in order to record the loading history within it. Huespe *et al.* [1] model the early stages of continuous casting, namely the mould and a small portion of the secondary cooling region, by taking a portion of the strand as long as the domain of interest and following it from the instant it reaches the meniscus until it completely leaves the domain. Bellet and Heinrich global non-stationary approach [2] considers a material domain that continuously increases, driven by a fictitious extraction tool. Once the fictitious tool has traversed a given section of the caster, this section tends to the steady state. Although the objective is to simulate continuous casting processes in steady state, both approaches need to perform a transient analysis until reaching stationarity making them computationally expensive.

Such inconvenience is usually overcome by restricting the analysis to a thin transverse slice of the strand, giving rise to the so-called slice models. A slice is assumed to be subject to simplified boundary conditions on its top and bottom surfaces. The most frequent assumption is that of generalized plane strain (GPS), which implies constant strain in the out-of-plane directions. Following Risso *et al.* [3], we will use henceforth the denomination extended plane strain (EPS) instead of GPS, because the latter was used in the literature to designate a kinematic hypothesis in plate analysis.

The EPS slice model has been the most popular way of analysing continuous casting processes from the early one-dimensional models, such as the analytical model of Weiner and Boley [4] widely used for validation purposes. Numerical models based on this approach were proposed by Rammerstorfer *et al.* [5], Kristiansson [6], Thomas and coworkers [7–11], and recently Pascon *et al.* [12], Li and Thomas [13], and Risso *et al.* [3]. Alternatively, some models make use of simpler kinematic hypothesis: plane strain conditions have been assumed by Funk and coworkers [14–16], Lee *et al.* [17], Han *et al.* [18], and Park *et al.* [19, 20]. Plane stress was often assumed in earlier works, like those of Williams *et al.* [21], Lewis *et al.* [22], and Thomas *et al.* [23–25], who turned later to EPS models they considered more realistic.

However, in a process in which boundary conditions and especially temperatures (responsible for thermal strains and variations in the mechanical properties of the material) change markedly, the simplified boundary conditions applied to the transverse slice model yield quite a crude approximation of reality. Indeed, our experience in modelling the early stages of continuous casting processes began with the plane-strain slice model [26], which was soon abandoned because of accuracy considerations, and replaced by Lagrangian [1] and Arbitrary Lagrangian–Eulerian (ALE) [27] models, where the domain of analysis embodied the whole region of interest from the

DOI: 10.1002/nme

meniscus to a certain distance below the mould such that the strain state at the mould exit, known to be a critical section, was properly modelled. Actually, the displacement field computed with the slice model [26] differs from those obtained with Lagrangian [1] and ALE [27] models to an extent comparable to the gap between the billet and the mould, one of the main variables in the coupled thermomechanical analysis of continuous casting processes.

On the other hand, the Eulerian approach—based on spatial points—is particularly appropriate for modelling flows through a spatially fixed region such as the process we are interested in. However, Eulerian evolution equations are more difficult to integrate than Lagrangian's because state variables are not associated to spatial points but to material points. Therefore, Eulerian-formulated rate equations include an advective term that requires special treatment when numerical methods are used. Such drawback has prevented the application of pure Eulerian schemes to the continuous casting process.

Among the schemes where the mesh is attached to the caster, we can mention the works of Sorimachi *et al.* [28] and Kelly *et al.* [29]. In these works, the thermal loads are applied incrementally and therefore a sort of transient problem has to be solved. The material being inelastic, a non-linear problem must be solved at each temperature increment which makes this model as expensive as non-slice Lagrangian models.

A mixed Eulerian–Lagrangian approach is proposed in this work, in order to retain the advantages of both formulations: the boundary values problem for stress distribution is formulated over the points inside a fixed region of the caster (Eulerian formulation), while the constitutive equations are stated over the material points passing through this region (Lagrangian approach). The history of the particle occupying a sampling point of the analysed region at a given instant will be built by tracking the particle along its streamline from the molten region to the sampling point. This is the so-called streamline integration method [30], where the streamline computation becomes trivial because of the physics of the continuous casting process: (i) the strand is just slightly deformed from its original cylindrical shape (small strains assumption) and (ii) the velocity associated to the deformation of the strand is negligible with respect to the advection velocity of the solid particles. Then, we can assume all the solid particles move with uniform axial velocity, coinciding with the casting velocity. As it will be shown later, by using this strategy the mechanical analysis of a steady-state continuous casting process truly remains a steady-state problem.

The examples are particularly devoted to the simulation of the early stages of round billet continuous casting. The considered region contains the mould and a few water sprays in the secondary cooling zone. An axial-symmetric model is used for the simulation, after assuming this region to be straight. However, we remark that the same technique can be applied in three-dimensional cases.

2. LAGRANGIAN FORMULATION OF THE CONSTITUTIVE EQUATIONS

According to the local state theory [31], the thermodynamic state at any particle $\mathbf{X}$ of a material medium at a given instant t is completely defined by the values of a certain number of state variables at this particle at this instant. Computations on inelastic materials take advantage of strain-driven formulations, in which state variables are the total strain $\boldsymbol{\varepsilon}$ and a set of phenomenological internal strain-type variables describing material history, together with the temperature field T here assumed to be known *a priori*.

DOI: 10.1002/nme

Since maximum strains are expected to be below 2% [32], small strains theory can be applied to describe deformations during continuous casting processes. Then, the total strain can be additively decomposed as follows

$$\boldsymbol{\varepsilon} = \boldsymbol{\varepsilon}^{\mathrm{e}} + \boldsymbol{\varepsilon}^{\mathrm{i}} \tag{1}$$

$\boldsymbol{\varepsilon}^{\mathrm{e}}$ being the elastic (reversible) strain including thermal expansion and $\boldsymbol{\varepsilon}^{\mathrm{i}}$ the inelastic (irreversible) strain. Either term may play the role of an internal variable, but $\boldsymbol{\varepsilon}^{\mathrm{i}}$ is typically chosen (as in this work).

We also adopt a scalar internal variable α, which characterizes isotropic hardening from the phenomenological point of view. The hypothesis of isotropic hardening is widely accepted in continuous casting applications [33]. Furthermore, the most popular choice for the hardening parameter α relies on the equivalent inelastic strain:

$$\alpha = \int_0^t \sqrt{\frac{2}{3}}\, \|\dot{\boldsymbol{\varepsilon}}^{\mathrm{i}}(\tau)\|\, \mathrm{d}\tau \tag{2}$$

where $\dot{\boldsymbol{\varepsilon}}^{\mathrm{i}}$ is the inelastic strain rate and $\|\dot{\boldsymbol{\varepsilon}}^{\mathrm{i}}\| = \sqrt{\dot{\varepsilon}^{\mathrm{i}}_{ij}\dot{\varepsilon}^{\mathrm{i}}_{ij}}$ its L_2-norm.

Although driving variables lie in strain space, response functions (i.e. the yield criterion and the evolution laws) are usually written in terms of their conjugated thermodynamic forces: the stress tensor $\boldsymbol{\sigma}$ (dual of $\boldsymbol{\varepsilon}$ or $\boldsymbol{\varepsilon}^{\mathrm{i}}$) and the isotropic hardening variable in stress space, $R = R(\alpha)$.

The stress tensor $\boldsymbol{\sigma}$ depends on $\boldsymbol{\varepsilon}$ and $\boldsymbol{\varepsilon}^{\mathrm{i}}$ through the decomposition (1). For linearly elastic isotropic materials, the stress is defined by the state law:

$$\boldsymbol{\sigma} = \mathbf{C}(\boldsymbol{\varepsilon}^{\mathrm{e}} - \boldsymbol{\varepsilon}^{0}) \tag{3}$$

where $\boldsymbol{\varepsilon}^0$ is the initial strain field, and $\mathbf{C} = \lambda \mathbf{l} \otimes \mathbf{l} + 2\mu \mathbf{I}$ is the fourth-order tensor of elastic moduli, $\mathbf{l}$ being the second-order unit tensor with components δ_{ij} (the Kronecker delta), $\mathbf{I}$ the fourth-order unit tensor with components $I_{ijkl} = (\delta_{ik}\delta_{jl} + \delta_{il}\delta_{jk})/2$; $\lambda = \lambda(T)$ and $\mu = \mu(T)$ are thermal-dependent material properties known as Lamé constants, which can be determined in terms of the elastic (or Young's) modulus $E = E(T)$ and Poisson ratio $\nu = \nu(T)$ as $\lambda = \nu E/[(1 + \nu)(1 - 2\nu)]$ and $\mu = E/[2(1 + \nu)]$.

Let us decompose the stress tensor as follows:

$$\boldsymbol{\sigma} = \mathbf{s} + p\mathbf{l} \tag{4}$$

$\mathbf{s} = \mathrm{dev}(\boldsymbol{\sigma})$ being the deviatoric stress and $p = \frac{1}{3}\,\mathrm{tr}\,(\boldsymbol{\sigma})$ the mean stress. From Equation (3), the following constitutive equations for $\mathbf{s}$ and p are derived:

$$\mathbf{s} = 2\mu\, \mathrm{dev}(\boldsymbol{\varepsilon}^{\mathrm{e}} - \boldsymbol{\varepsilon}^{0}), \quad p = \kappa\, \mathrm{tr}\,(\boldsymbol{\varepsilon}^{\mathrm{e}} - \boldsymbol{\varepsilon}^{0}) \tag{5}$$

where $\kappa = \lambda + 2\mu/3$ is the bulk modulus.

Regarding the initial strain field $\boldsymbol{\varepsilon}^0$, it is composed of the thermal strain $\boldsymbol{\varepsilon}_{\mathrm{T}}$ and a strain $\boldsymbol{\varepsilon}^0_{\mathrm{s}}$ that corresponds to the state a particle has just before developing mechanical strength. Under the small-strain assumption, such decomposition can be written as follows:

$$\boldsymbol{\varepsilon}^0 = \boldsymbol{\varepsilon}_{\mathrm{T}} + \boldsymbol{\varepsilon}^0_{\mathrm{s}} \tag{6}$$

DOI: 10.1002/nme

The thermal strain is defined as

$$\boldsymbol{\varepsilon}_{\mathrm{T}} = \mathrm{TLE}(T)\mathbf{I} \quad \text{with } \mathrm{TLE}(T) = \int_{T_{\mathrm{ref}}}^{T} \alpha_{\mathrm{T}}(\tau)\,\mathrm{d}\tau \tag{7}$$

TLE denoting the thermal linear expansion function, α_{T} the linear thermal expansion coefficient and T_{ref} an arbitrary reference temperature.

The von Mises criterion, for the time being the most widely yield criterion used for metals, is defined as follows:

$$f = \|\mathbf{s}\| - \sqrt{\tfrac{2}{3}}\,[\sigma_{\mathrm{Y}} + R(\alpha)] \tag{8}$$

where σ_{Y} is the initial yield stress and R measures the isotropic hardening in the stress space.

Associated to this yield criterion, the following J_2 flow rule is considered:

$$\dot{\boldsymbol{\varepsilon}}^{\mathrm{i}} = \gamma \mathbf{n} \tag{9}$$

$\mathbf{n} = \mathbf{s}/\|\mathbf{s}\|$ being the normalized stress deviator defining the normal to the Von Mises yield surface $f = 0$ in the deviatoric-stress space and $\gamma \geqslant 0$ the consistency parameter. For plastic materials, γ is determined by means of the consistency condition

$$\gamma \dot{f} = 0 \tag{10}$$

On the other hand, viscoplastic (rate dependent) materials require a constitutive equation for γ. In this work, the following law is proposed:

$$\gamma = \frac{1}{\eta} g(f)\xi(\alpha) \tag{11}$$

where $\eta = \eta(T)$ is the material viscosity, g is a non-negative, monotonically increasing function of f, such that $g = 0$ if and only if $f \leqslant 0$, and $\xi = \xi(\alpha)$ is the multiplicative-viscosity hardening term. The constitutive equation (11) allows us to encompass all the 'standard' viscoplastic models described by Lemaître and Chaboche [31], either with isotropic hardening or no hardening at all (perfect viscoplasticity). For instance, by neglecting $\xi(\alpha)$, we recover the Lemaître and Chaboche's additive-viscosity hardening model, originally proposed by Perzyna [34].

Finally, having chosen the equivalent inelastic strain as hardening variable, the flow rule (9) results

$$\dot{\alpha} = \sqrt{\tfrac{2}{3}}\,\|\dot{\boldsymbol{\varepsilon}}^{\mathrm{i}}\| = \sqrt{\tfrac{2}{3}}\,\gamma \tag{12}$$

completely defining the hardening law.

3. INTEGRATION OF THE EVOLUTION EQUATIONS

Following Simo and Hughes [35], we discretize the evolution laws (9) and (12) using the implicit Euler-backward finite-difference scheme. Then, given the total strain increment $\Delta\boldsymbol{\varepsilon}$ at the particle $\mathbf{X}$ during the time interval $[t_n, t_{n+1}]$, $t_{n+1} = t_n + \Delta t$, the material state at $\mathbf{X}$ is updated from the

DOI: 10.1002/nme

previous instant t_n to the current one t_{n+1} as follows:

$$\boldsymbol{\varepsilon}(\mathbf{X}, t_{n+1}) = \boldsymbol{\varepsilon}(\mathbf{X}, t_n) + \Delta\boldsymbol{\varepsilon} \tag{13}$$

$$\boldsymbol{\varepsilon}^{\mathrm{i}}(\mathbf{X}, t_{n+1}) = \boldsymbol{\varepsilon}^{\mathrm{i}}(\mathbf{X}, t_n) + \Delta\gamma(\mathbf{X}, t_{n+1})\mathbf{n}(\mathbf{X}, t_{n+1}) \tag{14}$$

$$\alpha(\mathbf{X}, t_{n+1}) = \alpha(\mathbf{X}, t_n) + \sqrt{\tfrac{2}{3}}\,\Delta\gamma(\mathbf{X}, t_{n+1}) \tag{15}$$

with $\Delta\gamma \doteq \gamma\Delta t$.

Let $\mathbf{X}^0, \mathbf{X}^1, \ldots, \mathbf{X}^n$ be the particles currently occupying those positions (with respect to a fixed reference frame) of $\mathbf{X}$ at the previous points $t_0 = 0, t_1, \ldots, t_n$ of the time discretization, i.e.

$$\mathbf{x}(\mathbf{X}, t_j) = \mathbf{x}(\mathbf{X}^j, t_{n+1}), \quad j = 0, 1, \ldots, n \tag{16}$$

Therefore, under steady-state conditions, the history of $\mathbf{X}$ may be traced by recording the current state at the particles $\mathbf{X}^j$:

$$\boldsymbol{\varepsilon}^{\mathrm{i}}(\mathbf{X}, t_j) = \boldsymbol{\varepsilon}^{\mathrm{i}}(\mathbf{X}^j, t_{n+1}) \tag{17}$$

$$\alpha(\mathbf{X}, t_j) = \alpha(\mathbf{X}^j, t_{n+1}) \tag{18}$$

The initial state at $\mathbf{X}$, coinciding with the current state at $\mathbf{X}^0$, is assumed to be known. In continuous casting, it corresponds to the completely liquid material, where all the internal variables vanish:

$$\boldsymbol{\varepsilon}^{\mathrm{i}}(\mathbf{X}, t_0) = \boldsymbol{\varepsilon}^{\mathrm{i}}(\mathbf{X}^0, t_{n+1}) = \mathbf{0} \tag{19}$$

$$\alpha(\mathbf{X}, t_0) = \alpha(\mathbf{X}^0, t_{n+1}) = 0 \tag{20}$$

Now, using Equations (17)–(20), the discrete evolutionary equations (14) and (15) can be completely stated at the current instant t_{n+1}:

$$\boldsymbol{\varepsilon}^{\mathrm{i}}(\mathbf{X}, t_{n+1}) = \sum_{j=1}^{n+1} \Delta\gamma(\mathbf{X}^j, t_{n+1})\mathbf{n}(\mathbf{X}^j, t_{n+1}) \tag{21}$$

$$\alpha(\mathbf{X}, t_{n+1}) = \sqrt{\frac{2}{3}} \sum_{j=1}^{n+1} \Delta\gamma(\mathbf{X}^j, t_{n+1}) \tag{22}$$

where $\mathbf{X}^{n+1} \equiv \mathbf{X}$.

4. EULERIAN FORMULATION OF THE BOUNDARY VALUE PROBLEM

The standard quasi-static boundary value problem in solid mechanics, stated in mixed $\mathbf{u}$–p form [36], consists in finding the displacement field $\mathbf{u}$ and the mean-stress field p that satisfy

DOI: 10.1002/nme

the integral equations

$$\int_\Omega \mathrm{tr}\,(\mathbf{s}\,\mathrm{grad}\,\mathbf{w})\,\mathrm{d}V + \int_\Omega p\,\mathrm{div}\,\mathbf{w}\,\mathrm{d}V = \int_\Omega \rho\mathbf{b}\cdot\mathbf{w}\,\mathrm{d}V + \int_{\partial\Omega_\sigma} \bar{\mathbf{t}}\cdot\mathbf{w}\,\mathrm{d}S \tag{23}$$

$$\int_\Omega \left[\mathrm{tr}\,(\boldsymbol{\varepsilon}-\boldsymbol{\varepsilon}^0) - \frac{p}{\kappa}\right] q\,\mathrm{d}V = 0 \tag{24}$$

throughout the domain Ω, for all the admissible displacement and mean-stress weighting functions $\mathbf{w}$ and q, respectively.

Equation (23) is the weak form of the momentum balance equations, where $\rho\mathbf{b}$ is the body-force (per unit volume) and $\bar{\mathbf{t}}$ is the traction prescribed over the portion $\partial\Omega_\sigma$ of the boundary (displacement boundary conditions over the complementary portion $\partial\Omega_u$ are assumed to hold *a priori*). Inertial effects are ignored in momentum balance according to the assumption of constant and uniform velocity field within the solid.

Equation (24) is the weighted residual form of the linear thermal-elastic constitutive equation (5) for the mean stress p. The classical hypothesis of isochoric inelastic deformation, i.e.

$$\mathrm{tr}\,(\boldsymbol{\varepsilon}^{\mathrm{i}}) = 0 \tag{25}$$

which is implied by the J_2 flow rule (9), is called for in Equation (24).

4.1. Finite element approximation

Appropriate mixed finite elements should be employed in order to deal with the numerical difficulties eventually caused by the inelastically incompressible behaviour of metals. We refer to the classical finite element literature [36, 37] for a detailed discussion of admissible **u**- and p-shape functions that guarantee the fulfilment of the Babuška–Brezzi stability conditions.

The displacement and mean-stress trial functions are defined as follows:

$$\mathbf{u} = \sum_{i=1}^{n_u} N_i\mathbf{U}_i = \mathbf{N}\mathbf{U} \tag{26}$$

$$p = \sum_{j=1}^{n_p} N_{p_j} P_j = \mathbf{N}_p\mathbf{P} \tag{27}$$

N_i being the displacement shape function associated to the displacement node $i = 1, 2, \ldots, n_u$, $\mathbf{U}_i$ the nodal displacement, N_{p_i} the mean-stress shape function associated to the mean-stress node $j = 1, 2, \ldots, n_p$, and P_j the nodal mean stress.

After replacing **u** and p by their respective finite element approximations, and by adopting the corresponding shape functions as weight functions (Galerkin formulation), it yields

$$\mathbf{R}_1 = \mathbf{F}_{\mathrm{int}} - \mathbf{F}_{\mathrm{ext}} = \mathbf{0} \tag{28}$$

$$\mathbf{R}_2 = \mathbf{K}_p^{\mathrm{T}}\mathbf{U} - \mathbf{M}_p\mathbf{P} - \mathbf{F}_0 = \mathbf{0} \tag{29}$$

DOI: 10.1002/nme

where

$$\mathbf{F}_{\text{int}} = \int_{\Omega} \mathbf{B}^{\mathrm{T}} \mathbf{s}\, \mathrm{d}V + \mathbf{K}_p \mathbf{P} \tag{30}$$

$$\mathbf{F}_{\text{ext}} = \int_{\Omega} \mathbf{N}^{\mathrm{T}} \rho \mathbf{b}\, \mathrm{d}V + \int_{\partial\Omega_\sigma} \mathbf{N}^{\mathrm{T}} \bar{\mathbf{t}}\, \mathrm{d}S \tag{31}$$

$$\mathbf{K}_p = \int_{\Omega} \mathbf{B}^{\mathrm{T}} \mathbf{l} \mathbf{N}_p\, \mathrm{d}V \tag{32}$$

$$\mathbf{M}_p = \int_{\Omega} \frac{1}{\kappa} \mathbf{N}_p^{\mathrm{T}} \mathbf{N}_p\, \mathrm{d}V \tag{33}$$

$$\mathbf{F}_0 = \int_{\Omega} \mathrm{tr}\,(\boldsymbol{\varepsilon}^0) \mathbf{N}_p^{\mathrm{T}}\, \mathrm{d}V \tag{34}$$

In the above equations $\mathbf{B}$ is the typical finite element matrix defining the strain–displacement kinematics relation

$$\boldsymbol{\varepsilon} = \mathbf{B}\mathbf{U} \tag{35}$$

while symmetric second-order tensors like the stress deviator $\mathbf{s}$ and the unit tensor $\mathbf{l}$ are mapped into vectors as usually done in the finite element practice.

4.2. Computation of strains and stresses

Due to the small strains hypothesis, Eulerian and Lagrangian strain and stress tensors actually coincide. So, the Lagrangian version of Equations (23) and (24) is identical in form to the Eulerian's, but the integration domain Ω is different. While the domain of analysis Ω is a fixed portion of the strand moving down the caster for Lagrangian formulations (and, therefore, Ω is submitted to transient conditions), with Eulerian formulations Ω becomes a spatially fixed region attached to the caster. We choose the latter approach, which is especially advantageous because of the steady state developed into the spatially fixed domain Ω.

Let $\mathbf{x}$ be the fixed position of a typical sampling point within Ω, as well as the position of the particle $\mathbf{X}$ at time t_{n+1}:

$$\mathbf{x} = \mathbf{x}(\mathbf{X}, t_{n+1}) \tag{36}$$

Let us now take a snapshot of every Lagrangian field at the current instant t_{n+1} in order to obtain the corresponding Eulerian field, e.g.

$$\tilde{\boldsymbol{\varepsilon}}(\mathbf{x}) = \mathbf{B}(\mathbf{x})\mathbf{U} = \boldsymbol{\varepsilon}(\mathbf{X}, t_{n+1}) \tag{37}$$

$$\tilde{\boldsymbol{\varepsilon}}^{\mathrm{i}}(\mathbf{x}) = \boldsymbol{\varepsilon}^{\mathrm{i}}(\mathbf{X}, t_{n+1}) \tag{38}$$

$$\tilde{\alpha}(\mathbf{x}) = \alpha(\mathbf{X}, t_{n+1}) \tag{39}$$

etc. The tilde identifies frozen Eulerian fields. From now on, we will work with fields of this kind, omitting the tilde for conciseness.

DOI: 10.1002/nme

The (Cauchy) stress deviator at $\mathbf{x}$, equal to the (nominal) stress deviator at $\mathbf{X}$ at t_{n+1}, takes the form

$$\mathbf{s} = 2\mu(T)\,\mathrm{dev}(\boldsymbol{\varepsilon} - \boldsymbol{\varepsilon}^0 - \boldsymbol{\varepsilon}^{\mathrm{i}}) \tag{40}$$

The predictor–corrector algorithm known as return mapping [35] will be used to update the material state. First, we define the trial state (solution of the predictor problem) by assuming a completely elastic deformation at $\mathbf{X}$ during the period $[t_n, t_{n+1}]$. Then, the trial inelastic strain at $\mathbf{X}$ at t_{n+1} coincides with the inelastic strain at this particle at t_n, i.e. with the current inelastic strain at the particle $\mathbf{X}^n$:

$$\boldsymbol{\varepsilon}^{\mathrm{i,\ trial}}(\mathbf{x}) = \boldsymbol{\varepsilon}^{\mathrm{i}}(\mathbf{X}, t_n) = \boldsymbol{\varepsilon}^{\mathrm{i}}(\mathbf{X}^n, t_{n+1}) = \boldsymbol{\varepsilon}^{\mathrm{i}}(\mathbf{x}^n) \tag{41}$$

where $\mathbf{x}^j = \mathbf{x}(\mathbf{X}^j, t_{n+1})$, $\mathbf{x}^{n+1} \equiv \mathbf{x}$. Now, the trial deviatoric stress may be written as follows:

$$\mathbf{s}^{\mathrm{trial}}(\mathbf{x}) = 2\mu(T(\mathbf{x}))\,\mathrm{dev}(\boldsymbol{\varepsilon}(\mathbf{x}) - \boldsymbol{\varepsilon}^0(\mathbf{x}) - \boldsymbol{\varepsilon}^{\mathrm{i}}(\mathbf{x}^n)) \tag{42}$$

Trial and real states are related by the expression:

$$\mathbf{s} = \mathbf{s}^{\mathrm{trial}} - 2\mu(T)\Delta\gamma\mathbf{n} \tag{43}$$

Both tensors, $\mathbf{s}$ and $\mathbf{s}^{\mathrm{trial}}$, are collinear, that is

$$\mathbf{n} = \frac{\mathbf{s}}{\|\mathbf{s}\|} = \frac{\mathbf{s}^{\mathrm{trial}}}{\|\mathbf{s}^{\mathrm{trial}}\|} \tag{44}$$

hence Equation (43) yields

$$\|\mathbf{s}\| = \|\mathbf{s}^{\mathrm{trial}}\| - 2\mu\Delta\gamma \tag{45}$$

The latter equation shows that the corrector step leading to the real state reduces itself to the determination of the consistency parameter γ by invoking either the consistency requirement (10) for plastic materials or the constitutive equation (11) for standard viscoplastic ones.

4.3. Newton–Raphson method

The non-linear system of Equations (28) and (29) is solved iteratively. To this end, let us approximate this system at the kth iteration using a linear Taylor expansion

$$\mathbf{R}^{(k)} = \mathbf{R}^{(k-1)} + \mathbf{K}^{(k-1)} \underbrace{(\mathbf{d}^{(k)} - \mathbf{d}^{(k-1)})}_{\Delta\mathbf{d}^{(k)}} = \mathbf{0} \tag{46}$$

$\mathbf{R}$ and $\mathbf{d}$ being the residue and unknown vectors, respectively, and $\mathbf{K}$ the tangent matrix, given by

$$\mathbf{R} = \begin{bmatrix} \mathbf{R}_1 \\ \mathbf{R}_2 \end{bmatrix}, \quad \mathbf{d} = \begin{bmatrix} \mathbf{U} \\ \mathbf{P} \end{bmatrix}, \quad \mathbf{K} = \frac{\mathrm{d}\mathbf{R}}{\mathrm{d}\mathbf{d}} = \begin{bmatrix} \mathbf{K}_D & \mathbf{K}_p \\ \mathbf{K}_p^{\mathrm{T}} & -\mathbf{M}_p \end{bmatrix} \tag{47}$$

The submatrices $\mathbf{K}_p$ and $\mathbf{M}_p$ in $\mathbf{K}$ are defined by Equations (32) and (33), and

$$\mathbf{K}_D = \frac{\partial \mathbf{R}_1}{\partial \mathbf{U}} = \int_\Omega \mathbf{B}^{\mathrm{T}} \frac{\partial \mathbf{s}}{\partial \mathbf{U}}\,\mathrm{d}V \tag{48}$$

DOI: 10.1002/nme

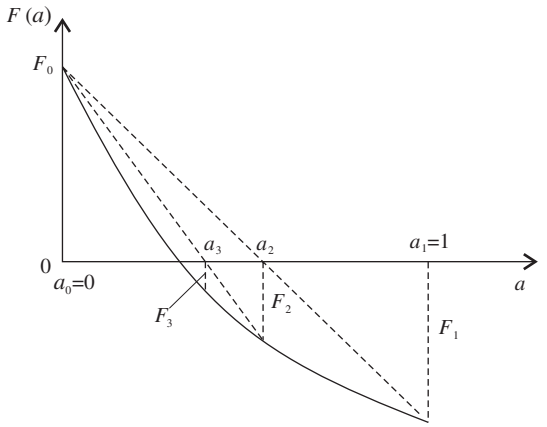

Figure 1. Iterative computation of the line-search parameter a using the regula-falsi method.

The Newton–Raphson technique gives a quadratic asymptotic rate of convergence provided the initial guess $\mathbf{d}^0$ lies within the zone of attraction of the final solution [38]. Otherwise, the iterative guess $\mathbf{d}^k$ must be forced to reach this zone. Here, a line-search algorithm is implemented to this end. Thus, $\Delta\mathbf{d}$ in Equation (46) is not assumed to define the increment of $\mathbf{d}$ but the searching direction. The new guess $\mathbf{d}^{(k)}$ is then defined as

$$\mathbf{d}^{(k)} = \mathbf{d}^{(k-1)} + a\Delta\mathbf{d}^{(k)} \tag{49}$$

where a ($0<a\leqslant 1$) is a parameter controlling the step size, which is determined so that the projection of the residue $\mathbf{R}$ onto the search direction $\Delta\mathbf{d}$ be minimized (if possible).

4.3.1. Line-search algorithm. The parameter a in the previous equation is computed by means of the line-search algorithm [39]. At each iteration k, once $\Delta\mathbf{d}^{(k)}$ is known, the computation of a proceeds as follows:

- If $\|\mathbf{R}(\mathbf{d}^{(k-1)} + \Delta\mathbf{d}^{(k)})\| < \|\mathbf{R}(\mathbf{d}^{(k-1)})\|$, update $\mathbf{d}$ using Equation (49) with $a = 1$ and go to the next Newton–Raphson iteration.
- Otherwise, let

$$F(a) = \mathbf{R}(\mathbf{d}^{(k-1)} + a\Delta\mathbf{d}^{(k)}) \cdot \Delta\mathbf{d}^{(k)} \tag{50}$$

define the function to minimize in the interval $0<a\leqslant 1$.

— If $\text{sign}(F(0)) = \text{sign}(F(1))$, set $a = a_{\min}$ ($a_{\min} = 0.01$ for the current application), update $\mathbf{d}$ using Equation (49) and go to the next Newton–Raphson iteration.

— Otherwise, a is computed using the iterative regula-falsi (or secant) technique schematized in Figure 1. The process is stopped at a line-search iteration q for which F_q is below a given tolerance, we adopted equal to $0.01F(1)$. Then, we set $a = a_q$, update $\mathbf{d}$ using Equation (49) and go to the next Newton–Raphson iteration.

DOI: 10.1002/nme

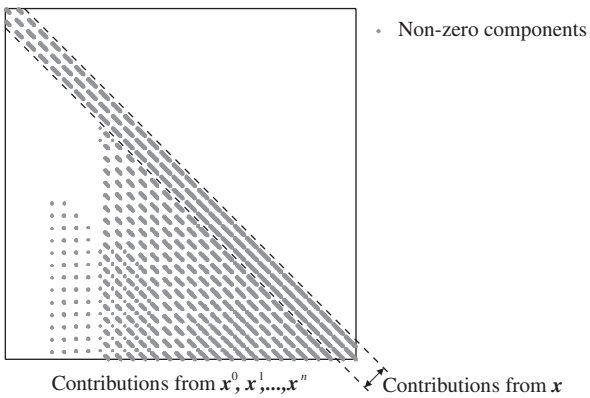

Figure 2. Typical sparsity pattern of the exact tangent matrix $\mathbf{K}_D$.

4.3.2. Computation of the tangent matrix. Computing the derivatives of the stress deviator $\mathbf{s}$ (mapped into a vector as usual in the finite element formulation) with respect to the nodal displacements, which appear in the integrand of the sub-matrix $\mathbf{K}_D$, is all that remains to be done in order to complete the definition of the tangent matrix $\mathbf{K}$. If we use indicial notation for convenience's sake, after differentiating Equation (40), we obtain:

$$\left.\frac{\partial s_{ij}}{\partial U_k}\right|_{\mathbf{x}} = \left[2\mu\left(I_{ijpq} - \frac{1}{3}\delta_{ij}\delta_{pq}\right)\frac{\partial \varepsilon_{pq}}{\partial U_k} - 2\mu\frac{\partial \varepsilon^{\mathrm{i}}_{ij}}{\partial U_k}\right]_{\mathbf{x}} \tag{51}$$

Using finite elements, the derivative of the total strains is determined by the gradient matrix $\mathbf{B}$. Regarding the derivative of the inelastic strain, differentiation of Equation (21) yields

$$\left.\frac{\partial \varepsilon^{\mathrm{i}}_{ij}}{\partial U_k}\right|_{\mathbf{x}} = \sum_{j=1}^{n+1}\left[n_{pq}\frac{\partial \Delta\gamma}{\partial U_k} + \Delta\gamma\frac{\partial n_{pq}}{\partial U_k}\right]_{\mathbf{x}^j} \tag{52}$$

with $\mathbf{x} \equiv \mathbf{x}^{n+1}$.

As it can be seen, after replacing Equation (52) into (51), and this one into (48), the tangent matrix $\mathbf{K}_D$ becomes non-symmetric and almost triangular because of the terms evaluated at points other than $\mathbf{x}$, which are located in different finite elements, as shown in Figure 2, which displays a typical sparsity pattern of the tangent matrix for applications like those presented in Sections 6 and 7, where structured rectangular meshes are used. A sparse solver that takes advantage of this particular pattern can be used, for instance, the LAPACK routines for LU factorization of sparse general matrices [40] after sparse column minimum degree permutation [41].

It can further be seen that if these terms are disregarded, we recover the symmetric banded tangent matrix of classical finite element analysis. Neglecting the contributions from some (even all) of the points $\mathbf{x}^j$ leads to an approximation of the tangent matrix $\mathbf{K}_D$. In that way we get a modified Newton–Raphson method, whose convergence is worse than that of the exact Newton–Raphson. However, the cost of solving the linear system (46) per iteration diminishes because the band-width of $\mathbf{K}_D$ diminishes.

DOI: 10.1002/nme

Standard viscoplastic model. Derivatives in the r.h.s. of Equation (52) take now the form:

$$\left.\frac{\partial \Delta\gamma}{\partial U_k}\right|_{\mathbf{x}} = \Theta(\mathbf{x})\left[n_{ij}(\mathbf{x})\left(\left.\frac{\partial \varepsilon_{ij}}{\partial U_k}\right|_{\mathbf{x}} - \left.\frac{\partial \varepsilon^{\mathrm{i}}_{ij}}{\partial U_k}\right|_{\mathbf{x}^n}\right) + \frac{1}{2\mu(T(\mathbf{x}))}\left(\theta(\mathbf{x}) - \sqrt{2/3}R'(\mathbf{x})\right)\left.\frac{\partial \alpha}{\partial U_k}\right|_{\mathbf{x}^n}\right] \tag{53}$$

$$\left.\frac{\partial n_{ij}}{\partial U_k}\right|_{\mathbf{x}} = \frac{2\mu(T(\mathbf{x}))}{\|\mathbf{s}^{\mathrm{trial}}(\mathbf{x})\|}\left(I_{ijpq} - \frac{1}{3}\delta_{ij}\delta_{pq} - n_{ij}(\mathbf{x})n_{pq}(\mathbf{x})\right)\left(\left.\frac{\partial \varepsilon_{pq}}{\partial U_k}\right|_{\mathbf{x}} - \left.\frac{\partial \varepsilon^{\mathrm{i}}_{pq}}{\partial U_k}\right|_{\mathbf{x}^n}\right) \tag{54}$$

where $(*)'$ stands for the derivative of the univariate function $(*)$—particularly, R' is the material hardening modulus—and

$$\theta = \frac{g\xi'}{g'\xi} \tag{55}$$

$$\Theta^{-1} = 1 + \frac{R'}{3\mu} + \frac{\eta}{2\mu g'\xi\Delta t} - \frac{\theta}{\sqrt{6}\mu} \tag{56}$$

Evaluation of Equations (53) and (54) at any other point $\mathbf{x}^j$ is straightforward: one only needs to replace $\mathbf{x} \equiv \mathbf{x}^{n+1}$ for $\mathbf{x}^j$ and $\mathbf{x}^n$ for $\mathbf{x}^{j-1}$.

Using Equations (52)–(54), Equation (51) can be recast for the viscoplastic model as follows:

$$\begin{aligned}\left.\frac{\partial s_{ij}}{\partial U_k}\right|_{\mathbf{x}} &= 2\mu(T(\mathbf{x}))\left[(1-\omega(\mathbf{x}))\left(I_{ijqp} - \frac{1}{3}\delta_{ij}\delta_{pq}\right) - \vartheta(\mathbf{x})n_{ij}(\mathbf{x})n_{pq}(\mathbf{x})\right]\left.\frac{\partial \varepsilon_{pq}}{\partial U_k}\right|_{\mathbf{x}} \\ &\quad -2\mu(T(\mathbf{x}))\left[(1-\omega(\mathbf{x}))I_{ijqp} - \vartheta(\mathbf{x})n_{ij}(\mathbf{x})n_{pq}(\mathbf{x})\right]\left.\frac{\partial \varepsilon^{\mathrm{i}}_{pq}}{\partial U_k}\right|_{\mathbf{x}^n} \\ &\quad -\Theta(\mathbf{x})(\theta(\mathbf{x}) - \sqrt{2/3}R'(\mathbf{x}))n_{ij}(\mathbf{x})\left.\frac{\partial \alpha}{\partial U_k}\right|_{\mathbf{x}^n}\end{aligned} \tag{57}$$

where

$$\omega = \frac{2\mu\Delta\gamma}{\|\mathbf{s}^{\mathrm{trial}}\|} = 1 - \frac{\|\mathbf{s}\|}{\|\mathbf{s}^{\mathrm{trial}}\|} \tag{58}$$

$$\vartheta = \Theta - \omega \tag{59}$$

Plastic model. The rate-independent formulation can be recovered from the previous rate-dependent model as the viscosity parameter η tends to zero. In that case, the inverse viscosity or fluidity η^{-1} playing the role of a penalty parameter, causes the states outside the loading surface $f = 0$ to be increasingly penalized so that f tends to zero; and $g(f)$ (a monotonically increasing function of f that vanishes for $f \leqslant 0$) also does so. Therefore, we only need to take $\theta = 0$ and

$$\Theta^{-1} = 1 + \frac{R'}{3\mu} \tag{60}$$

to fit the previous formulation to the plastic model.

DOI: 10.1002/nme

5. IMPLEMENTATION DETAILS

The present model will be applied to the simulation of the early stages of steel round billets continuous casting. As usual, such process will be studied assuming axial-symmetry conditions.

For the spatial discretization, we use quadratic-displacement constant-mean stress triangular finite elements (simply called $T6/1$ for having six **u**-nodes and one p-node). These elements are the simplest elements to fulfil the Babuška–Brezzi condition [42].

We further adopt a rectangular mesh with uniform element size h_z in the axial direction z. This choice is particularly advantageous in modelling steady-state continuous casting processes. First, since the particles within the solidified shell move in the axial direction with a velocity that is (up to an infinitesimal term) equal to the given constant casting velocity $\mathbf{V}_c$, the positions $\mathbf{x}^j$ previously occupied by the particle currently located at any sampling point $\mathbf{x}$ of the mesh can be determined immediately:

$$\mathbf{x}^j = \mathbf{x} - \mathbf{V}_c(t_{n+1} - t_j) \tag{61}$$

Having taken h_z constant, let us adopt a time step Δt such that the Courant number is a natural number

$$Co = \frac{\|\mathbf{V}_c\|\Delta t}{h_z} \in \mathbb{N} \tag{62}$$

the point $\mathbf{x}^j$ will also be a sampling point of the mesh. In that case, all the history of the particle occupying a sampling point at any point of the time discretization will be recorded in other sampling points to avoid the need of interpolating the internal variables and the undesired numerical diffusion introduced by such interpolation.

The present mechanical model is restricted to the solid material. The liquid material is just modelled as a metallostatic pressure boundary condition applied on the solid–liquid interface. In this context, let us point out that the terms 'solid' and 'liquid' stand for material zones whose temperature is respectively below and above the zero-strength temperature (ZST), defined to be the minimum temperature at which the material exhibits no strength [43, 44], although in general it does not coincide with the solidification temperature (in low carbon steels, this temperature corresponds to solid fractions of 0.6–0.8 [43, 44]).

The present strategy, which is based on using a rectangular mesh, hinders the accurate meshing of the solid domain adjacent to the solid–liquid interface. However, if the mesh is fine enough, we can discard the elements traversed by this interface without affecting the accuracy of the whole solution, as shown in Figure 3. This reduces therefore the computational cost but requires special care when dealing with the pressure boundary condition at the interface: the stress state in a particle at the beginning of the solidification is equal to the ferrostatic pressure at the solid–liquid interface (in fact, this pressure is negligible during the early stages of the continuous casting process, so that a just-solidified particle must be stress free). This condition serves for determining $\boldsymbol{\varepsilon}_s^0$, which must make up the difference between the total and the thermal strains in the liquid elements, as suggested by Thomas and Parkman [11]. Due to the particular discretization strategy we have adopted, this condition is shifted up to the first solidified sampling point $\mathbf{x}^0$, so that its value is

$$\boldsymbol{\varepsilon}_s^0 = \boldsymbol{\varepsilon}(\mathbf{x}^0) - \varepsilon_T(\mathbf{x}^0)\mathbf{I} \tag{63}$$

and remains constant all along the trajectory beginning at $\mathbf{x}^0$.

DOI: 10.1002/nme

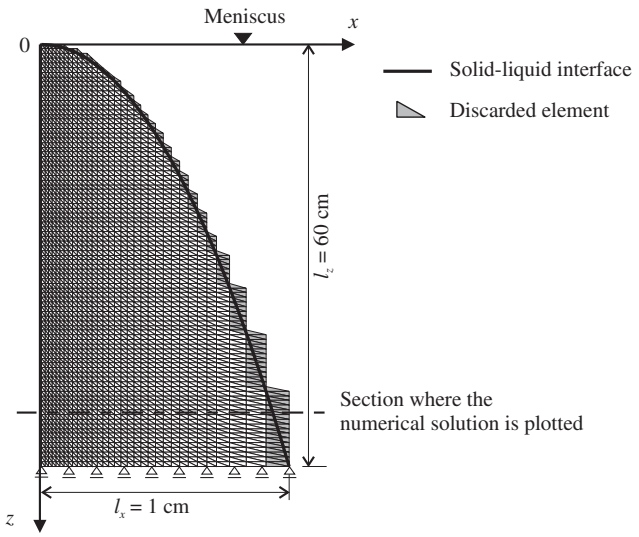

Figure 3. Finite element mesh and boundary conditions for Weiner and Boley's [4] validation problem with $\lambda = 0.4$ and $m = 0.06$.

Let us remark that the use of a rectangular mesh with uniform mesh size in the casting direction clearly simplifies the implementation of the model for the simulation of the early stages of continuous casting process, assuming the caster to be straight or just slightly curved. But in fact it is not compulsory to have neither a straight domain nor a structured mesh. All we need to know *a priori* is the streamlines (up to an infinitesimal term due to deformation) in order to determine the successive positions of the particles. For continuous casting applications, and keeping in mind that we consider only the solidified shell, this may be possible even in the case of a curved caster. Concerning the use of an unstructured mesh, the history of a particle occupying a sampling point at a given instant will not be recorded anymore in other sampling points. This requires to project the internal variables to the previous positions of the particle, as usually done when other ALE methods are used (see for instance the ALE formulation for solidification problems proposed by Bellet and Fachinotti [45]), but does not prevent in any way the use of this model with such meshes.

6. VALIDATION

A simplified problem concerning the development of thermal stresses in a solidifying slab is solved for validation purposes. This is an idealization of the early stage of solidification in a continuous casting square mould, whose analytical solution was proposed by Weiner and Boley [4]. The material is a pure metal with melting point T_s, that is initially liquid at a uniform temperature $T_0 = T_s$ (i.e. there is no superheat). The mould (at $x = 0$) is maintained at a uniform temperature $T_m < T_s$ and perfect thermal contact is assumed between the mould and the slab, so that solidification begins immediately.

DOI: 10.1002/nme

Table I. Thermomechanical and process parameters for the Weiner and Boley's [4] validation problem with $\lambda = 0.4$ and $m = 0.06$.

Melting point	$T_s = 1490°C$
Mould temperature	$T_m = 1362°C$
Density	$\rho = 7200\ \mathrm{kg/m^3}$
Latent heat of solidification	$L = 272\,000\ \mathrm{J/kg}$
Specific heat	$c_p = 680\ \mathrm{J/(kg°C)}$
Thermal conductivity	$k_s = 34\ \mathrm{W/(m°C)}$
Thermal diffusivity	$\kappa_s = \frac{k_s}{\rho c_p} = 6.944 \times 10^{-6}\ \mathrm{m^2/s}$
Elastic modulus	$E = 40\,000\ \mathrm{MPa}$
Poisson ratio	$\nu = 0.35$
Initial yield stress at T_m	$Y_0 = 40\ \mathrm{MPa}$
Thermal expansion coefficient	$\alpha_T = 8.46354 \times 10^{-5}/°C$
Reference temperature for thermal expansion	$T_{ref} = 1490°C$
Casting velocity	$\|\mathbf{V}_c\| = 1.6\ \mathrm{m/min}$

The domain of analysis consists of the section of the solidified shell lying on the longitudinal mid-plane, taken to be coincident with the xz-plane. For small time t ($t = 0$ corresponds to the initial condition $T = T_0$), the thermal field in this region is closely approximated by Neumann's solution for the solidification in a semi-infinite slab (see [46, pp. 285–286] for details). Then, the thickness of the solidified shell at time t is given by

$$l_s = 2\lambda\sqrt{\kappa_s t} \tag{64}$$

where κ_s is the thermal diffusivity in the solid and λ is a real constant.

Weiner and Boley [4] presented results for some particular values of λ. We adopted $\lambda = 0.4$ for the purpose of making a comparison. As $\lambda^2 \ll 1$, the following relationship holds [4]:

$$\lambda = \sqrt{\frac{c_s(T_s - T_m)}{2L}} \tag{65}$$

where c_s is the heat capacity of the solid, and L is the latent heat per unit mass. Then, knowing the material properties c_s, T_s and L, we adjust the mould temperature T_m in order to get $\lambda = 0.4$ (see Table I).

Now, the temperature at time t can be computed as

$$T(\hat{x}, t) = T_m + D(T_s - T_m)\,\mathrm{erf}(\lambda\hat{x}), \quad 0 \leqslant \hat{x} \leqslant 1 \tag{66}$$

where we introduce the dimensionless abscissa $\hat{x}(t) = x/l_s(t)$ and constant $D = 1/\mathrm{erf}(\lambda)$ (the above solution was actually obtained under the hypothesis of similarity [46]).

In the context of continuous casting, assuming that the strand moves in z-direction with a constant velocity $\mathbf{V}_c$, let us change the time variable t by the z-co-ordinate using the relationship

$$z = \|\mathbf{V}_c\| t \tag{67}$$

The level $z = 0$ corresponds to the meniscus.

Then, we build a mesh of a rectangular box of height l_z (equal to the mould length) and width l_x (equal to the shell thickness at $z = l_z$), so that it contains the solidified region defined by Equation

DOI: 10.1002/nme

(64) inside the mould. Such mesh consists of rectangular $T6/1$ finite elements, with uniform size h_z in z-direction. For $l_z = 0.6$ m, we adopt $h_z = l_z/90$ and $Co = 1$, which determine a time step $\Delta t = 0.25$ s. At $z = l_z$, there are 33 finite elements in the x-direction, their sizes ranging from 6.8 mm at $x = 0$ to 4.7 cm at $x = l_x$. Each node of the mesh is assigned a temperature determined by Equation (66). Please note that only the elements with all their nodes having a temperature below T_s are considered.

Model geometry and boundary conditions as well as the location of the T_s-isotherm (solid–liquid interface) are depicted in Figure 3.

The material is assumed to be elastic–perfectly plastic, with a initial yield stress $\sigma_Y = \sigma_Y(T)$ defined by

$$\sigma_Y = Y_0 \frac{T_s - T}{T_s - T_m} \tag{68}$$

where Y_0 is the initial yield stress at the mould temperature T_m.

Now, let us introduce the following dimensionless stress:

$$\hat{\sigma}_{ij} = \frac{(1-\nu)\sigma_{ij}}{\alpha_T E(T_s - T_m)} \tag{69}$$

Weiner and Boley obtained the following similarity solution for the variation of $\hat{\sigma} = \hat{\sigma}_{yy} = \hat{\sigma}_{zz}$ ($\hat{\sigma}_{xx} = 0$) along the shell thickness:

$$\hat{\sigma} = \begin{cases} m[D\,\mathrm{erf}(\lambda\hat{x}) - 1], & 0 \leqslant \hat{x} < \hat{x}_2 \\ m[1 - D\,\mathrm{erf}(\lambda\hat{x}_1)] + D[\mathrm{erf}(\lambda\hat{x}_1) - \mathrm{erf}(\lambda\hat{x})] & \\ \quad -\dfrac{2}{\sqrt{\pi}} D(1-m)\lambda\hat{x}_1 \exp(-\lambda^2\hat{x}_1^2) \log\dfrac{\hat{x}_1}{\hat{x}}, & \hat{x}_2 \leqslant \hat{x} \leqslant \hat{x}_1 \\ m[1 - D\,\mathrm{erf}(\lambda\hat{x})], & \hat{x}_1 < \hat{x} \leqslant 1 \end{cases} \tag{70}$$

where

$$m = \frac{(1-\nu)Y_0}{\alpha_T E(T_s - T_m)} \tag{71}$$

and the abscissas $\hat{x}_1$ and $\hat{x}_2$, $\hat{x}_2 < \hat{x}_1$, are determined by solving the non-linear system of equations:

$$\begin{cases} 2(1-m)\lambda^2\hat{x}_1(\hat{x}_1 - \hat{x}_2)\exp(-\lambda^2\hat{x}_1^2) \\ \quad = (1+m)\exp(-\lambda^2\hat{x}_2^2) - (1-m)\exp(-\lambda^2\hat{x}_1^2) - m[\exp(-\lambda^2) + 1] \\ \dfrac{2}{\sqrt{\pi}}(1-m)\lambda\hat{x}_1 \exp(-\lambda^2\hat{x}_1^2)\log\dfrac{\hat{x}_1}{\hat{x}_2} = (1-m)\,\mathrm{erf}(\lambda\hat{x}_1) - (1+m)\,\mathrm{erf}(\lambda\hat{x}_2) + 2m\,\mathrm{erf}\,\lambda \end{cases} \tag{72}$$

In the region $\hat{x} < \hat{x}_2$ (close to the cooled surface) the material exhibits plastic behaviour and is subject to compression; from $\hat{x} = \hat{x}_2$ to $\hat{x} = \hat{x}_1$ there is a region of elastic unloading where the stress change of sign; in the region $\hat{x} > \hat{x}_1$ (close to the solid–liquid interface) the material behaves as a plastic and is under tension. As for λ, Weiner and Boley results correspond to some values of m. Here, we choose $m = 0.06$ and adjust the material parameters in Table I to this end. Solving Equation (72) for $m = 0.06$ and $\lambda = 0.4$, we obtain $\hat{x}_1 = 0.4527$ and $\hat{x}_2 = 0.2140$.

DOI: 10.1002/nme

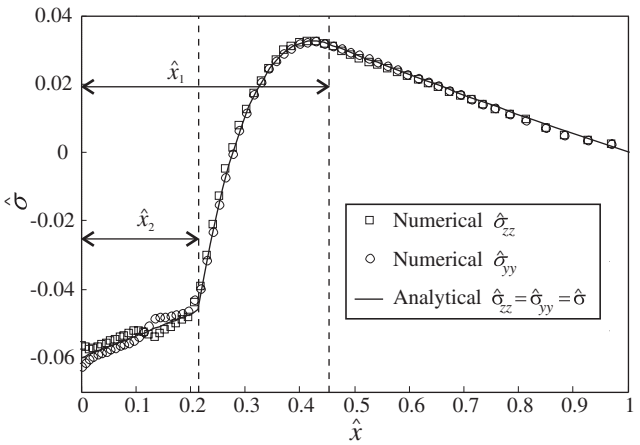

Figure 4. Finite element vs analytical computed stresses for Weiner and Boley's [4] validation problem with $\lambda = 0.4$ and $m = 0.06$.

Figure 4 shows good agreement between the numerical computed stress components $\hat{\sigma}_{yy}$ and $\hat{\sigma}_{zz}$ and the analytical one σ^*. The section from which the numerical solutions were taken corresponds to $z = 50$ cm. The slight difference observed in the plastic zone next to the chilled surface is attributed to the steps of the stair-shaped mesh in the proximity of the meniscus. This deviation associated to the spatial discretization is considered an admissible numerical error for the purpose of the current analysis.

7. INDUSTRIAL APPLICATION

Let us model the early stages of the continuous casting of steel round billets. The analysed domain Ω goes from the meniscus to a short distance below the mould, as shown in Figure 5. The curvature of the strand will be ignored and the process is assumed to have axial symmetry. The finite element mesh of the solidified portion of the domain is shown in Figure 6. The uniform mesh size in the axial direction is $h_z = 6.667$ mm, so that, assuming $Co = 1$, the time step size is $\Delta t = 0.25$ s.

7.1. Thermal solution

The numerical computation procedure of the thermal field in continuous casting processes has been described in a previous work [47]. The material data used in this analysis is listed in Table II.

Concerning boundary conditions, the meniscus and the bottom surfaces are adiabatic, while heat is extracted through the external surface of the shell according to the following laws:

$$q_{\text{mould}} = 3.071 - 0.361\sqrt{t} \quad \text{along the billet–mould interface} \tag{73}$$

$$q_{\text{sprays}} = h(T - T_{\text{ext}}) \quad \text{along the surface subjected to water spraying} \tag{74}$$

DOI: 10.1002/nme

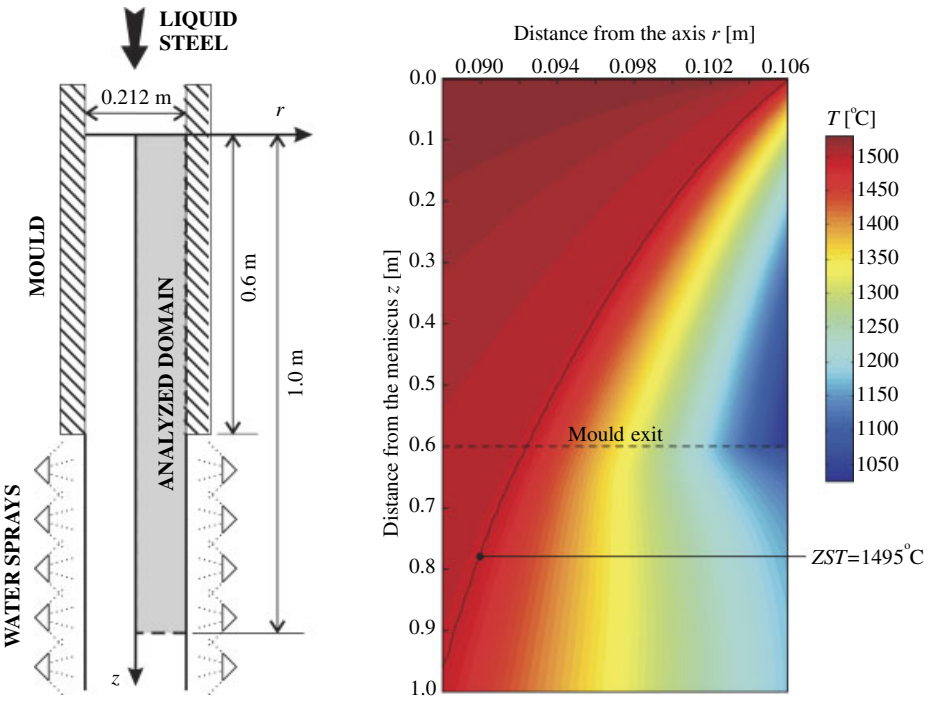

Figure 5. Steel round billet continuous casting process. Schematized geometry and temperature within the analysed domain.

where q_{mould} is given in MW/m^2 for $t = z/\|\mathbf{V}_c\|$ in seconds, h is the heat convection coefficient and T_{ext} the temperature of the environment in the sprays zone (see Table II). Equation (73) is a Savage–Pritchard law, whose coefficients were obtained by means of an inverse analysis for the conditions met in plant [48].

Let us remark that, unlike mechanical analysis, thermal analysis concerns the solid as well as the liquid sub-domains of Ω. The model of phase change used here is of fixed-mesh type [47] takes into account the phase change is of fixed-mesh type, i.e. the heat exchange in the solidification front is implicit in the weak form of the heat equation and does not need to be treated explicitly as a boundary condition.

The resulting temperature distribution in Ω is plotted in the right of Figure 5.

7.2. *Plastic model*

The cast steel will be modelled first as a plastic material with linear isotropic hardening, i.e.

$$R(\alpha) = K(T)\alpha \tag{75}$$

where K $(= R')$ is the material hardening modulus. All the mechanical properties for this model were taken from the work of Rugonyi *et al.* [49] (except the TLE function, extracted from Reference [29]), and are listed in Table III. Rugonyi *et al.* fitted Wray's experimental data [50] for a strain rate of 1.5×10^{-4} s^{-1} they considered as characteristic of the process.

Figure 7 shows the tensile curves for this material, at high temperatures.

DOI: 10.1002/nme

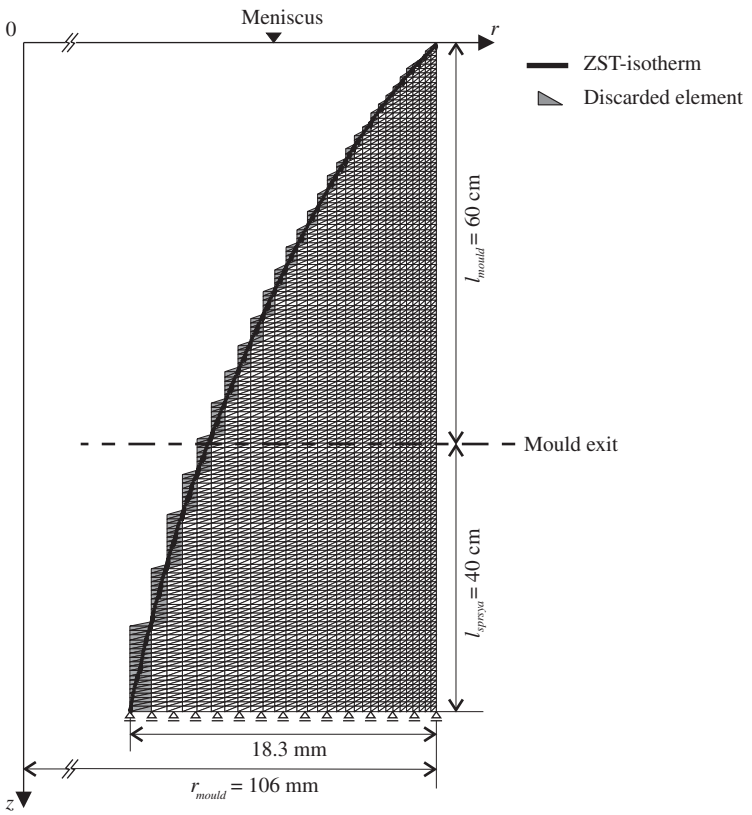

Figure 6. Steel round billet continuous casting process. Finite element mesh for the stress analysis.

Table II. Thermal properties for the steel round billet continuous casting simulation.

Pouring temperature	1530°C
Zero-strength temperature	ZST = 1495°C
Solidus temperature	1490°C
Liquidus temperature	1501°C
Liquid fraction	Linear between solidus and liquidus
Density	7200 kg/m^3
Latent heat of solidification	$L = 272\,000$ J/kg
Specific heat	$c_p = 680$ J/(kg°C)
Thermal conductivity in solid	34 W/(m°C)
Thermal conductivity in liquid	68 W/(m°C)
Casting velocity	$\|\mathbf{V}_c\| = 1.6$ m/ min
Convection coefficient in the sprays zone	$h = 500$ W/(°C m^2)
External temperature in the sprays zone	$T_{ext} = 40$°C

DOI: 10.1002/nme

Table III. Plastic model of a medium-carbon steel: thermal-dependent mechanical properties.

T (°C)	E (MPa)	v	σ_Y (MPa)	K (MPa)	TLE
900	32 378	0.33	14.0	160	−0.01326
1000	20 000		11.0		
1100	14 542		8.0		
1200	12 896		5.5	160	−0.00675
1300	11 954	0.33	4.0	80	
1400	8068	0.36	3.5	50	
1416				40	−0.00200
1450	5062	0.40	1.9		
1490	97	0.41	0.5	7	−0.00029
1495	2	0.41	0.5	7	0.00000

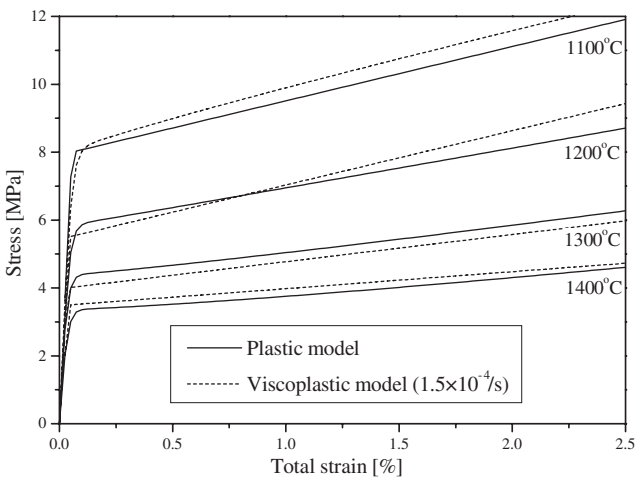

Figure 7. Tensile curves for the plastic and viscoplastic models at elevated temperatures.

7.3. Standard viscoplastic model

We now describe the behaviour of steel using the classical Perzyna model [34], which is a standard viscoplastic model with additive-viscosity hardening. Therefore, the multiplicative-hardening term $\xi(\alpha)$ in Equation (11) is set to one. This model was proposed by Huespe *et al.* [51] as the multiaxial generalization of Kozlowski *et al.*'s one-dimensional model III [32]. This model assumes:

$$g = \tfrac{1}{2}(f + |f|)^N \tag{76}$$

$$\eta = (2/3)^{(N+1)/2} C^{-1} \exp \frac{Q}{kT(^\circ\mathrm{C})} \tag{77}$$

$$\sigma_Y = 0 \tag{78}$$

$$R(\alpha) = K\alpha^M \tag{79}$$

DOI: 10.1002/nme

the latter defining the Ramberg–Osgood non-linear hardening law [31]. The parameters in the above equations, taken from Reference [32], are given by

$$N = 8.132 - 1.540 \times 10^{-3} T \ (^{\circ}\mathrm{C}) \tag{80}$$

$$C = 46\,550 + 71\,400c + 12\,000c^2 \tag{81}$$

$$\frac{Q}{k} = 44\,650 \tag{82}$$

$$K = 130.5 - 5.128 \times 10^{-3} T \ (^{\circ}\mathrm{C}) \tag{83}$$

$$M = -0.6289 + 1.114 \times 10^{-3} T \ (^{\circ}\mathrm{C}) \tag{84}$$

where c is the steel carbon content in percentage (here, assumed equal to 0.3).

Also according to Kozlowski *et al.* [32], the following formula for the thermal-dependent elastic modulus is considered:

$$E = 960\,800 - 2330T + 1.9T^2 - 5.18 \times 10^{-4} T^3 \tag{85}$$

The other material properties, such as Poisson ratio and TLE function, are the same as those of the previous plastic model (Table III).

As seen in Figure 7, at the elevated temperatures involved in continuous casting, the tensile curves for this material agree quite well with those of the previous plastic model when the strain rate is $1.5 \times 10^{-4}\ \mathrm{s}^{-1}$ (the characteristic value assumed by Rugonyi *et al.* [49]).

7.4. Stress and strains solution

Figure 8 shows the radial displacement of the shell surface for $\Delta t = 0.25$ s ($Co = 1$), as computed using both the plastic and viscoplastic models of the previous paragraph. There is very good agreement between both curves. In fact, the maximum difference between them is about $1/1000$ the maximum radial displacement and is located at the mould exit. Let us remark that the interfacial gap

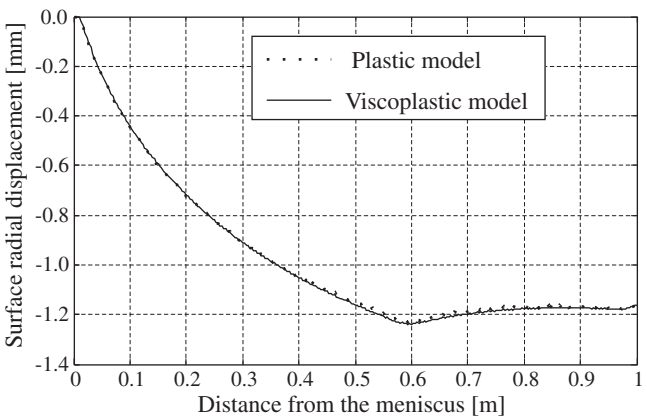

Figure 8. Radial displacement of the external surface.

DOI: 10.1002/nme

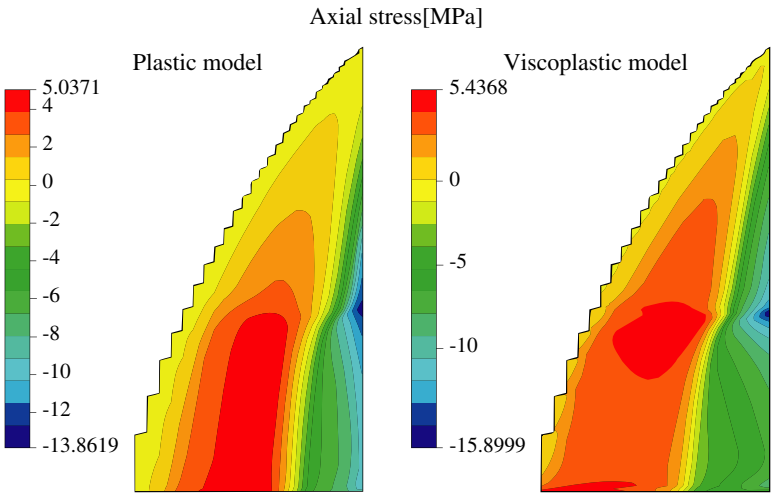

Figure 9. Axial stresses within the solidified shell.

that forms between the strand and the mould, which has fundamental influence on the strand cooling conditions inside the mould, is usually one-order-of-magnitude smaller than the displacement. In consequence, the material model, either dependent or not on strain rate, is not determinant in gap computations.

Axial stresses are plotted in Figure 9. The viscoplastic model predicts maximum compressive and tensile stresses that are slightly higher than those computed using the plastic model. But the more relevant difference between plastic and viscoplastic models is that observed in the zone of maximal tensile stresses at the mould exit. The viscoplastic model allows stress relaxation so that the region of maximal tension extends to a short distance below the mould (the high tension zone at the bottom of the domain is a numerical error introduced by blocking the axial displacement of the bottom nodes). On the other hand, the maximal tension zone predicted by the plastic model continues all along the analysed domain. This difference has important consequences on cracking prediction, as it will be pointed out later.

Regarding the other stress components, hoop stresses are very close to axial ones either for plastic or viscoplastic models, the radial and shear stresses were not significant throughout the domain.

Figure 10 plots the equivalent inelastic strain α. Plastic and viscoplastic models give similar results, with no significant inelastic strain developed inside the mould. Maximal inelastic strains are located at the shell surface along the sprays region, where compressive axial and hoop stresses are formed. Considering that the zones exhibiting high inelastic strains in addition to high tensile stresses are susceptible to cracking, the region located at the shell surface along the sprays region should not be affected since, as observed in Figure 9, main stresses in this zone are compressive. On the contrary, the region of high inelastic strain near the solidification front coincides with regions of tensile stresses in Figure 9. At this point, the differences between plastic and viscoplastic models in the extension of the regions of highest tensile stresses become very important. In fact, the highest tension and high inelastic strain are observed at the bottom of the domain using the plastic model, indicating possible cracking. On the other hand, using viscoplastic model, thanks to the stress

DOI: 10.1002/nme

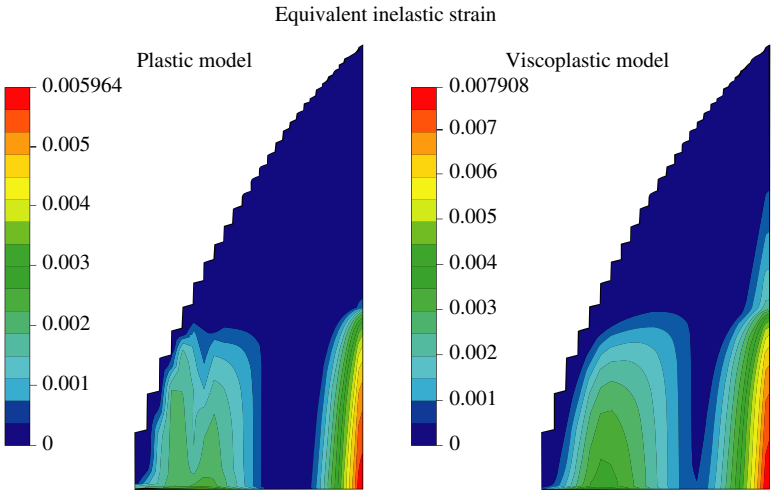

Figure 10. Equivalent inelastic strains within the solidified shell.

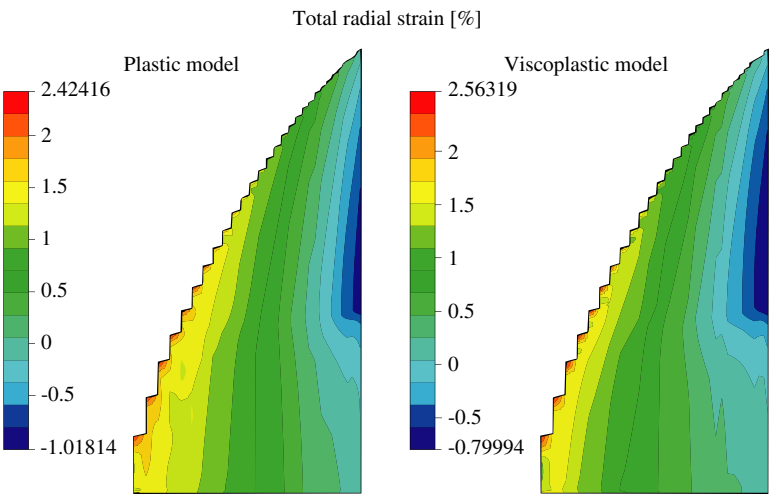

Figure 11. Total radial strains within the solidified shell.

relaxation phenomenon, the highest tension develops before the inelastic strain becomes high, so that no cracking is expected.

Even if the viscoplastic model is more sophisticated when it comes to phenomena such as relaxation which the plastic model ignores, and hence the viscoplastic solution is in theory more accurate than the plastic one, there is no experimental data to support this conclusion.

Finally, Figure 11 serves for validating the hypothesis of small strains assumed all along this work. Actually, the tensile radial strains adjacent to the solidification front shown in this figure are the highest strains in magnitude throughout the solidified domain. Although higher than 2%,

DOI: 10.1002/nme

the maximal value predicted by Kozlowski *et al.* [32], these strains are in the range of validity of the small-strain theory ($|\varepsilon_{ij}|<$2-to-5%, according to Lemaître and Chaboche [31]). On the other hand, no significant differences between plastic and viscoplastic models are observed in strain solutions.

7.5. Performance of the non-linear equation solver

The non-linear system of Equations (28) and (29) has been solved using either the exact or the modified Newton–Raphson method. The former implies the exact computation of the tangent matrix, while the latter assumes certain approximation of this matrix. Here, the tangent matrix is approximated by neglecting some of the terms associated to the previous points $\mathbf{x}^j$ occupied by the particle currently located at the considered sampling point $\mathbf{x}$.

Figure 12 shows the evolution of the residue norm $\|\mathbf{R}\| = \sqrt{\mathbf{R} \cdot \mathbf{R}}$ throughout the iterative solution process, assuming plastic behaviour and $Co = 1$ (in this case, a reduced mesh of bilinear quadrilateral elements was employed, but the results concerning convergence capability are quite general). The theoretical quadratic convergence rate of Newton–Raphson method is effectively attained when the matrix is computed exactly. Regarding the modified Newton–Raphson method, fewer history points are considered for computing the approximate tangent matrix, and more iterations are needed to achieve convergence. The maximum number of iterations corresponds to the case of symmetric approximation to the tangent matrix, without taking into account contributions from previous points.

At certain Newton–Raphson iterations, line search was used to improve convergence (this is done when we detect that the residual norm at the next iteration will increase). The number of iterations of the line-search cycle is typically two, so that the cost of the overall Newton–Raphson iteration does not increase too much with the line search.

However, as the approximation is improved by taking more previous points along particle streamlines, the computational cost per iteration (CPU-time and memory consumption) increases

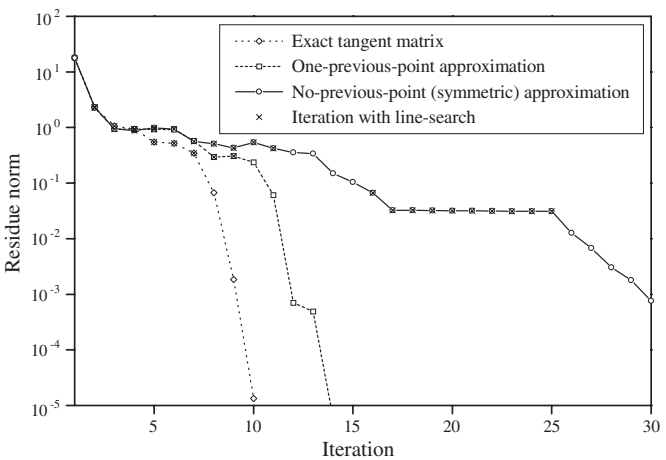

Figure 12. Evolution of the residue norm.

DOI: 10.1002/nme

since the band-width of the non-symmetric coefficient matrix increases accordingly. Therefore, there is a compromise between convergence rate and cost per iteration, which depends on the available computer resources.

Note that the cost per iteration corresponding to the symmetric case is comparable to that of other schemes of similar accuracy (this excludes the slice model, in which accuracy is deteriorated), such as the Lagrangian and the ALE techniques previously implemented by the authors (References [1, 27], respectively). Such methods require as many analyses as time steps taken for the time discretization, each analysis requiring a certain number of iterations. For instance, in order to solve the problem mentioned in this section, assuming $\Delta t = 0.25$ s, 150 analyses must be performed. If we assume each one takes typically 4–6 iterations [1, 27] to reduce the residue norm to 10^{-4} times its initial value (corresponding to a completely null displacement field), we get a total of 600–900 iterations. Meanwhile, the proposed Eulerian–Lagrangian technique just needs to consider a single time step, taking about 30 iterations to reach convergence with the same error tolerance when the symmetric approximation is used, so that it is an order of magnitude cheaper than the other schemes. Furthermore, the savings in computational cost increase as the time discretization becomes finer.

8. CONCLUSIONS

We have proposed a method for the analysis of stresses and strains developed in the solid region of a metal strand during continuous casting processes. By formulating the constitutive equations over the material particles (Lagrangian approach), we do not need to consider advection effects whose treatment can be cumbersome when numerical methods are used. On the other hand, by formulating the boundary value problem in Eulerian co-ordinates, the discretized domain remains fixed, coinciding with the region of interest within the continuous caster.

The present scheme, unlike the widely used slice model, does not need to simplify the kinematics at the transverse sections, allowing a better modelling of the variable conditions encountered by each material particle as it moves down the caster, and especially when it passes from one to another stage of the casting process (as it happens in current applications at the mould exit).

Besides, the evolution equations were formulated in a single time instant, which avoids the need to perform as many analyses as time steps taken for the time discretization. So, the computational cost involved in the proposed technique is considerably lower than that of other techniques with similar accuracy. Moreover, the advantages of using it increase as the number of time steps increases.

Finally, the non-linear governing equations are solved using either the exact Newton–Raphson method, which guarantees quadratic convergence rate, or its modified version, based on approximations to the tangent matrix. Among these approximations, we have the classical symmetric coefficient matrix. A line search algorithm was implemented in order to improve convergence.

Future work concerns the application of this model to a wider region of the caster, including particularly the secondary cooling zone, and to completely general three-dimensional processes, which involves curved casters, with consideration of lack of symmetry due to casters defects (misalignment of sprays, rolls, etc.).

DOI: 10.1002/nme

ACKNOWLEDGEMENTS

Financial support from Agencia Nacional de Promoción Científica y Tecnológica, Argentina, through grant PID 99-76, from Consejo Nacional de Investigaciones Científicas y Técnicas, through grant PIP 5271, and from Universidad Nacional del Litoral, through grant CAI + D PE 214, is gratefully acknowledged.

REFERENCES

1. Huespe AE, Cardona A, Fachinotti VD. Determinación de tensiones térmicas en aceros, producidas en la etapa inicial del proceso de colada continua. In *Mecánica Computacional* 1997; **XVIII**:185–194.
2. Bellet M, Heinrich A. A two-dimensional finite element thermomechanical approach to a global stress–strain analysis of steel continuous casting. *ISIJ International* 2004; **44**(10):1686–1695.
3. Risso JM, Huespe AE, Cardona A. Thermal stress evaluation in the steel continuous casting process. *International Journal for Numerical Methods in Engineering* 2006; **65**(9):1355–1377.
4. Weiner JH, Boley BA. Elasto-plastic thermal stresses in a solidifying alloy. *Journal of the Mechanics and Physics of Solids* 1963; **11**:145–154.
5. Rammerstorfer FG, Jaquemar Ch, Fischer DF, Wiesinger H. Temperature fields, solidification progress and stress development in the strand during a continuous casting process of steel. In *Numerical Methods in Thermal Problems*, Lewis RW, Morgan K (eds). Pineridge Press: Swansea, 1979; 712–722.
6. Kristiansson JO. Thermal stresses in the early stage of solidification of steel. *Journal of Thermal Stresses* 1982; **5**:315–330.
7. Moitra A, Thomas BG, Zhu H. Application of a thermo-mechanical model for steel behavior in continuous slab casting. *76th Steelmaking Conference*, Dallas, TX, March 1993; 657–667.
8. Lawson GD, Sander SC, Emling WH, Moitra A, Thomas BG. Prevention of shell thinning breakouts associated with widening width changes. *77th Steelmaking Conference*, Chicago, IL, Iron and Steel Society, Warrendale, PA, 1994; 329–336.
9. Thomas BG, Moitra A, Zhu H. Coupled thermo-mechanical model of solidifying steel shell applied to depression defects in continuous-cast slabs. *Modeling of Casting, Welding, and Advanced Solidification Processes VII*, London, September 1995.
10. Thomas BG, Moitra A, McDavid R. Simulation of longitudinal off-corner depressions in continuously cast steel slabs. *Iron and Steel Society's Process Technology Conference Proceedings*, Nashville, TN, vol. 13, 1996; 143–156.
11. Thomas BG, Parkman JT. Simulation of thermal mechanical behaviour during initial solidification. *Thermec '97 International Conference on Thermomechanical Processing of Steel and other Materials*, Wollongong, Australia, July 1997.
12. Pascon F, Habraken A-M, Bourdouxhe M, Labory F. Thermo-mechanical model of a strand in the mould in a continuous casting plant. *European Congress on Computational Methods in Applied Sciences and Engineering* (*ECCOMAS*), Barcelona, Spain, 2000.
13. Li Ch, Thomas BG. Thermo-mechanical finite element model of shell behavior in the continuous casting of steel. *6th Asia-Pacific Symposium on Engineering Plasticity and its Applications*, Sydney, Australia, December 2002; 827–834.
14. Bohemer JR, Fett FN, Funk G. Analysis of high-temperature behaviour of solidified material within a continuous casting machine. *Computers and Structures* 1993; **47**(4/5):683–698.
15. Funk G, Böhmer JR, Fett FN, Hentrich R. Coupled thermal and stress–strain models for the continuous casting of steels. *Steel Research* 1993; **64**(5):246–254.
16. Funk G, Boehmer JR, Fett FN. A coupled FDM/FEM model for the continuous casting process. *International Journal of Computer Applications in Technology* 1994; **7**(3–6):214–228.
17. Lee J-E, Han HN, Oh KH, Yoon J-K. A fully coupled analysis of fluid flow, heat transfer and stress in continuous round billet casting. *ISIJ International* 1999; **39**(5):435–444.
18. Han HN, Lee J-E, Yeo T-J, Won YM, Kim K-H, Oh KH, Yoon J-K. A finite element model for 2-dimensional slice of cast strand. *ISIJ International* 1999; **39**(5):445–454.
19. Park JK, Thomas BG, Samarasekera IV. Analysis of thermomechanical behaviour in billet casting with different mould corner radii. *Ironmaking and Steelmaking* 2002; **29**(5):1–17.
20. Park JK, Li Ch, Thomas BG, Samarasekera IV. Analysis of thermomechanical behaviour in billet casting. *60th Electric Furnace Conference*, San Antonio, TX, U.S.A., November 2002; 669–685.

DOI: 10.1002/nme

21. Williams JR, Lewis RW, Morgan K. An elasto-viscoplastic thermal stress model with applications to the continuous casting of metals. *International Journal for Numerical Methods in Engineering* 1979; **14**(1):1–10.
22. Lewis RW, Morgan K, Roberts PM. Determination of thermal stresses in solidification problems. In *Numerical Analysis of Forming Processes*, Chapter 15, Pittman JFT, Zienkiewicz OC, Wood RD, Alexander JM (eds). Wiley: New York, 1984; 405–431.
23. Thomas BG, Samaresekera IV, Brimacombe JK. Mathematical model of the thermal processing of steel ingots: Part II. Stress model. *Metallurgical Transactions B—Process Metallurgy* 1987; **18B**:131–147.
24. Thomas BG, Storkman WR, Moitra A. Optimizing taper in continuous slab casting molds using mathematical models. *6th International Iron and Steel Congress*, Nagoya, Japan, vol. 3, Iron and Steel Institute of Japan, October 1990; 348–355.
25. Moitra A, Thomas BG, Storkman W. Thermo-mechanical model of steel shell behavior in continuous casting mold. *TMS Annual Meeting*, San Diego, CA, March 1992.
26. Cardona A, Huespe A, Fachinotti V. Modelado termo-mecánico del proceso de colada continua de aceros. *Anales del XVIII Congresso Ibero Latino-Amer. de Mét. Comp. para Eng.* (*XVIII CILAMCE*), vol. I, Brasília: Brasil, 1997; 493–500.
27. Huespe AE, Cardona A, Fachinotti V. Thermomechanical model of a continuous casting process. *Computer Methods in Applied Mechanics and Engineering* 2000; **182**:439–455.
28. Sorimachi K, Susuki S, Imai T. Effects of thermal stresses on internal cracks in continuous casting of steel slabs. In *Numerical Methods in Thermal Problems*, Lewis RW, Morgan K (eds). Pineridge Press: Swansea, 1979; 703–711.
29. Kelly JE, Michalek KP, O'Connor TG, Thomas BG, Dantzig JA. Initial development of thermal and stress fields in continuously cast steel billets. *Metallurgical Transactions A—Physical Metallurgy and Materials Science* 1988; **19A**:2589–2602.
30. Agrawal A, Dawson PR. A comparison of Galerkin and streamline techniques for integrating strains from Eulerian flow fields. *International Journal for Numerical Methods in Engineering* 1985; **21**:853–881.
31. Lemaître J, Chaboche J-L. *Mechanics of Solid Materials*. Cambridge University Press: Cambridge, MA, 1994.
32. Kozlowski PF, Thomas BG, Azzi JA, Wang H. Simple constitutive equations for steel at high temperature. *Metallurgical Transactions A—Physical Metallurgy and Materials Science* 1992; **23A**:903–918.
33. Fachinotti VD, Cardona A. Constitutive models of steel under continuous casting conditions. *Journal of Materials Processing Technology* 2003; **135**:30–43.
34. Perzyna P. Thermodynamic theory of viscoplasticity. In *Advances in Applied Mechanics*, Yih C-S (ed.). vol. 11, Academic Press: New York, 1971; 313–354.
35. Simo JC, Hughes TJR. *Computational Inelasticity*. Springer: New York, 1998.
36. Hughes TJR. *The Finite Element Method. Linear Static and Dynamic Finite Element Analysis*. Prentice-Hall: Englewood Cliffs, NJ, 1987.
37. Zienkiewicz OC, Taylor RL. *The Finite Element Method*, *Volume 1*: *The Basis* (5th edn). Butterworth-Heinemann: Stoneham, MA, 2000.
38. Zienkiewicz OC, Taylor RL. *The Finite Element Method*, *Volume 2*: *Solid and Structural Mechanics* (5th edn). Butterworth-Heinemann: Stoneham, MA, 2000.
39. Matthies H, Strang G. The solution of nonlinear finite element equations. *International Journal for Numerical Methods in Engineering* 1979; **14**(11):1613–1626.
40. Anderson E, Bai Z, Bischof C, Blackford S, Demmel J, Dongarra J, Du Croz J, Greenbaum A, Hammarling S, McKenney A, Sorensen D. *LAPACK Users' Guide* (3rd edn). SIAM: Philadelphia, PA, 1999.
41. Gilbert JR, Moler C, Schreiber R. Sparse matrices in MATLAB: Design and implementation. *SIAM Journal on Matrix Analysis and Applications* 1992; **13**(1):333–356.
42. Arnold DN. Mixed finite element methods for elliptic problems. *Computer Methods in Applied Mechanics and Engineering* 1990; **82**:281–300.
43. Yamanaka A, Nakajima K, Okamura K. Critical strain for internal crack formation in continuous casting. *Ironmaking and Steelmaking* 1995; **22**(6):508–512.
44. Nakagawa T, Umeda T, Murata J, Kamimura Y, Niwa N. Deformation behavior during solidification of steels. *ISIJ International* 1995; **35**(6):723–729.
45. Bellet M, Fachinotti VD. Ale method for solidification modelling. *Computer Methods in Applied Mechanics and Engineering* 2004; **193**(39–41):4355–4381.
46. Carslaw HS, Jaeger JC. *Conduction of Heat in Solids* (2nd edn). Oxford University Press: Oxford, 1959.
47. Fachinotti V, Cardona A, Huespe A. Numerical simulation of conduction-advection problems with phase change. *Latin American Applied Research* 2001; **31**(1):31–36.

DOI: 10.1002/nme

48. Dvorkin E, Canga M. Thermomechanical behavior of the mold in Siderca continuous casting machine cc3. Case of ϕ 295 mm and carbon steel 042. *Technical Report I 1.20/190-90*, CINI, 1990.
49. Rugonyi S, Goldschmit M, Dvorkin E. Análisis numérico experimental de la CC3 de SIDERCA. informe de avance III. *Technical Report I-998/96*, CINI, 1996.
50. Wray PJ. Effect of carbon content on the plastic flow of plain carbon steels at elevated temperatures. *Metallurgical Transactions A—Physical Metallurgy and Materials Science* 1982; **13A**:125–134.
51. Huespe AE, Cardona A, Nigro N, Fachinotti V. Viscoplastic constitutive models of steel at high temperature. *Journal of Materials Processing Technology* 2000; **102**:143–152.

DOI: 10.1002/nme